The competition for salt and kinematic interactions between minibasins during density-driven subsidence: observations from numerical models.

Naiara Fernandez[a]*, Michael R. Hudec[a], Christopher A-L Jackson[b], Tim P. Dooley[a], Oliver B. Duffy[a]

[a]Bureau of Economic Geology, Jackson School of Geosciences, The University of Texas at Austin, University Station, Box X, Austin, Texas, 78713-8924, USA
[b]Basins Research Group (BRG), Department of Earth Science & Engineering, Imperial College, Prince Consort Road, London, United Kingdom, SW7 2BP, UK

**Corresponding author: naiara.fernandez@beg.utexas.edu*

Abstract

Stratal geometries of salt-floored minibasins provide a record of the interplay between minibasin subsidence and sedimentation. Minibasin subsidence and resulting stratal geometries are frequently interpreted by considering the minibasins in isolation and implicitly assuming that internal geometries are the result of purely vertical halokinetic processes. However, minibasins rarely form in isolation and may record complex subsidence histories even in the absence of tectonic forces. In this study we use numerical models to investigate how minibasins subside in response to density-driven downbuilding. We show that minibasins subsiding in isolation result in simple symmetric minibasins with relatively simple internal stratigraphic patterns. In contrast, where minibasins form in closely spaced arrays and subside at different rates, minibasins can kinematically interact due to complex patterns of flow in the encasing salt, even during simple density-driven subsidence. More specifically, we show that minibasins can: 1) prevent nearby minibasins from subsiding; 2) induce lateral translation of nearby minibasins; and 3) induce tilting and asymmetric subsidence of nearby minibasins. We conclude that even in areas where no regional or dominant salt flow regime exists, minibasins can still be genetically related and that minibasin subsidence histories cannot be fully understood if considered in isolation.

Introduction

Minibasins are small basins formed by subsiding into relatively thick autochthonous or allochthonous salt (e.g. Jackson and Hudec, 2017). Due to the specific properties of salt, which can flow under very low stresses, subsidence rates of minibasins can be orders of magnitude higher than subsidence rates in crustal basins, reaching values of up to 10,000 m/Myr (Worrall and Snelson, 1989). Because they can contain important thicknesses of sedimentary rocks that may include potential hydrocarbon reservoirs, minibasins have been widely studied in hydrocarbon-bearing salt basins (e.g. Hudec and Jackson, 2007).

The stratigraphic infill of minibasins provides a record of their subsidence histories. In simple terms, minibasin stratal geometries reflect the interplay between the two primary controls; minibasin subsidence and sediment accumulation. On the one hand, the bulk sediment accumulation rate is constrained by the sediment delivery system. On the other hand, the subsidence rate of a minibasin, which creates the accommodation space for new sediment, depends on minibasin geometry and density, and the patterns and vigor of salt flow below and around the minibasin (e.g. Hudec et al. 2009). As a result of the strong coupling between minibasin subsidence and sedimentation, changes in subsidence style are recorded by synkinematic stratal packages within minibasins (e.g. Giles and Lawton, 2002; Prather, 2003; Giles and Rowan, 2012; Sylvester et al., 2015; Jackson et al., 2019).

Based on 2D seismic reflection data from the northern Gulf of Mexico, Rowan and Weimer (1998) document different types of seismic-stratigraphic packages that can be linked to different styles of minibasin subsidence. Bowl- or layer-shaped symmetric packages record a broadly symmetric subsidence, while asymmetric subsidence and minibasin tilting result in wedge-shaped packages. In the simplest possible geometry, a minibasin that has a purely vertical subsidence history would be characterized by vertically stacked, symmetrical, bowl-shaped depocenters (Fig. 1A). Many other stratal geometries are possible though. For example a basal symmetric 'bowl' overlain by an asymmetric 'wedge' indicates and initially symmetric subsidence followed by minibasin tilting and subsequent asymmetric subsidence (Fig. 1B and C). Thus, minibasin depocenters do not necessarily stack vertically and need not be symmetrical, as they may be wedge-shaped and shift gradually or abruptly (Fig. 1B and C). The transition from a bowl- to a wedge-shaped package is interpreted by Rowan and Weimer (1998) as the timing of minibasin welding. However, Hudec et al. (2009) propose other non-welding related processes that can also lead to asymmetric subsidence, including the response to an asymmetric sediment load, syn-subsidence shortening and horizontal translation during canopy spreading.

Minibasin subsidence is commonly studied by considering the minibasin as an isolated element. Internal stratal geometries of isolated minibasins would passively record the interplay between the inflation of surrounding salt structures as the minibasin subsides, and the sediment accumulation in the minibasin (e.g. Koyi, 1998; halokinetic sequences, Giles and Lawton, 2002, Giles and Rowan, 2012). However, minibasins are rarely found in isolation, and are instead part of arrays of closely spaced minibasins bounded by complex networks of salt walls and diapirs forming minibasin provinces. Minibasin provinces form in different types of tectonic settings, ranging from collision zones such as the Precaspian and Sivas to passive margins such as the northern Gulf of Mexico and Brazil (e.g. Volozh et al., 2003; Callot et al., 2014 Worrall and Snelson, 1998; Fiduk and Rowan, 2012; Rowan and Vendeville, 2006). During shortening of minibasin provinces, contraction is preferably accommodated within the weaker salt and as a result, diapirs become squeezed or welded shut (e.g. Rowan and Vendeville, 2006). During their translation minibasins can interact with each other as they collide, jostle and/or slide past one another resulting in complex geometries (e.g. Rowan and Vendeville, 2006; Callot et al., 2016; Duffy et al., 2017). However, minibasins may still exhibit complex stratigraphic geometries indicative of complex subsidence histories in cases when shortening is not coeval with subsidence and/or where minibasins have not collided or are not welded laterally (e.g. Jackson et al., 2019). This is especially true in settings where adjacent minibasins can have very variable subsidence rates and where apparently isolated minibasins can still be filled by various sedimentary processes (e.g. continental basin-fill areas *sensu* Banham and Mountney, 2013) (Fig. 2). One question that has not been previously addressed explicitly is whether adjacent minibasins can influence each other and interact through salt flow without colliding or being welded together.

In this work we study the interactions between adjacent minibasins separated by diapirs subsiding into a homogenous salt layer with no regional tectonics (e.g. shortening) or dominant regional salt flow. For this purpose we perform a numerical modeling study that consists of several numerical simulations performed with a 2D finite-element code. The goal of this study is three-fold: first, to demonstrate that within arrays of minibasins subsiding at different rates, minibasins can influence adjacent ones by perturbing the salt flow around them; second, to observe and describe the different ways in which minibasin interactions can occur; third, to describe how minibasin stratal patterns record kinematic interactions between adjacent minibasin.

Numerical method and model setup

We use the 2D finite-element code MVEP2 (Thielmann and Kaus, 2012, Johnson et al., 2013). MVEP2 solves the equations of conservation of mass and momentum for incompressible materials with visco-elasto-plastic rheologies, and employs Matlab-based solvers MILAMIN (Dabrowski et al., 2008) for efficiency. The code uses a Lagrangian approach, where material properties are tracked by randomly distributed markers that are advected according to the velocity field that is calculated in a deformable numerical grid. Remeshing of the grid is performed every time step. The method and numerical implementation is explained in detail in Kaus, 2010.

In the simulations, 384 Lagrangian markers (hereinafter referred to as markers) are used per element to track the material properties, resulting in over 10 million markers in the modelled area. These markers have been perturbed from their initial regular position by applying random noise. The top, and left- and right-hand boundaries of the modelling domain have a free-slip boundary condition imposed, meaning that movement at the boundary can only occur parallel to the boundary. The bottom boundary of the domain has a no-slip boundary condition. An internal free-stress boundary is achieved by using the “sticky-air” layer approach (Crameri et al., 2012). This approach consists of adding a layer of zero density and relatively low viscosity (three orders of magnitude lower viscosity than salt phase) on top of the rock phases. By adding this layer, topography can develop at the interface between the “sticky-air” and rock phases (Fig. 4). Benchmark studies have shown that the ‘sticky air’ is a good approximation of a “free surface” (e.g. Crameri et al. 2012).

Two rock phases are used in the model: a phase corresponding to salt rock (e.g. halite) and one to sediments. Salt is modelled as a linear viscous fluid with a viscosity of 10^{18} Pa s (e.g. Mukherjee et al., 2010) and a density of 2200 kg/m^3 (i.e. halite). Sediments are modelled as visco-plastic materials, with a brittle rheology that is characterized by their cohesion (C) and effective friction angle (Φ). In the simulations, the color of the deposited sediments changes every 0.5 Myrs for visualization purposes only (i.e. there is no change in physical properties of the sediments associated with the color change).

Densities (ρ) of salt and sediment phases are modelled as constant and homogenous. Sediment density ($\rho_{sediment}$) is set higher than salt density, so that sediment-filled minibasins sink due to excess density. Sediments do not compact in the simulations presented here. This approach, results in density-driven subsidence of minibasins from the very beginning of the simulations, due to a gravity instability (density overturn) that has the added effect of sedimentation (e.g. Biot Ode, 1965; van Keken et al. 1993; Fernandez and Kaus, 2015). Assuming that minibasins are initiated by density-driven subsidence is a major simplification in areas where the minibasins are being filled with compacting siliciclastic sediments that would require a considerable thickness for the density overturn to occur (see Hudec et al., 2009). Thus, several mechanisms have been proposed in the literature to explain minibasin initiation and subsidence when sediments are less dense than the underlying salt (e.g. Hudec et al., 2009; Goteti et al., 2012). However, early density-driven subsidence of minibasins might be a valid assumption in areas where minibasins are being filled with denser than salt sediments (e.g. evaporitic and/or aeolian settings; Prochnow et al., 2006; Matthews et al., 2007; Pichat et al., 2019; see Fernandez et al., 2017). This is especially the case of evaporite-rich minibasins, whose 50-100% of infill is composed of evaporite-rich facies, and whose size tends to be smaller (e.g., 1-2 km wide) than their siliciclastic counterparts (see Fernandez et al., 2017 and Pichat et al., 2019). Additionally, the density-driven subsidence approach allows in our numerical models for minibasins to be initiated with no other additional process (e.g. shortening, sediment progradation, sustained sediment load; e.g. Hudec et al, 2009; Goteti et al., 2012), therefore simplifying the interpretation of the observed stratal geometries.

Sedimentation in the models is simulated by vertically displacing a horizontal reference level according to a specified aggradation rate (S) which in the numerical models is between 0.001 and 0.01 cm/year. For each time step, the model assumes that the depositing sediments fill the space up to the horizontal reference level. Therefore, the sediment accumulation rate and the thickness of each newly deposited layer in the model will depend both on the imposed aggradation rate and the subsidence of the underlying minibasin, the latter creating extra accommodation space (e.g. Fernandez and Kaus, 2015) (Fig. 3). Numerically, this process is implemented by converting any particle of "air-phase" below the reference-level to "sediment-phase" at each time step (Fig. 3). The resulting sediment accumulation rate in each of the minibasins of the simulations has been calculated based on the minibasin thickness variation between time steps. In the numerical simulations, the sediment accumulation rate is variable from minibasin to minibasin and through time. There is no erosion in the numerical simulations presented here.

Two geometric model setups were used: control simulations with a single seeded minibasin, and simulations with non-seeded arrays of minibasins (Fig. 4). Both setups start with an initial 1000 m thick flat layer of salt (Fig. 4). The control simulations for a single seeded minibasin have a simulation domain of 10 km wide by 4 km high (Fig.4). In these control simulations, an initial layer of sediments is added on top of salt at the center of the model. The purpose of this pre-kinematic layer is to help nucleate or seed a minibasin at the center of the modelling domain. The smaller model dimensions are enough to allow the formation of a single minibasin. This isolated minibasin subsides into a thick layer of salt unperturbed by any other minibasins. The modelling domain for simulations with non-seeded minibasin arrays is 30 km wide by 4 km high (Fig. 4). The model dimensions are enough to allow the formation and evolution of several km-scale minibasins and thus are appropriate to represent sub-domains of salt-tectonic systems containing minibasin arrays. This setup does not contain a pre-kinematic sediment layer on top of the salt, and thus minibasin position is not explicitly imposed during the simulations. Instead, minibasins develop spontaneously by density-driven subsidence and density overturn as sediments are added during the simulation (e.g. Fernandez and Kaus, 2015). The goal of the two setups is to compare the behavior and resulting stratal geometries of a single isolated minibasin to the behavior and geometries associated with minibasins subsiding as part of minibasin arrays.

Different sediment densities were used in the simulations with non-seeded minibasin arrays (Table 1). For each density, we performed a sensitivity study of sediment properties (C and Φ, Table 1). A total of 11 simulations of the single seeded minibasin setup and 112 simulations with the non-seeded minibasin arrays setup were performed. All the simulations within each geometrical setups have the position of the markers perturbed by the same noise (mean = - 0.0005 m; standard deviation = 0.9021 m; variance = 0.8137 m). The random noise causes heterogeneities of very small amplitude and wavelength in the salt-sediment interface in the initial stages. However, the heterogeneities are exactly the same in all the simulations within each of the geometrical setups. During the initial stages of the simulations, it is the heterogeneities with a wavelength closer to the dominant minibasin (or diapir) wavelength that get amplified and evolve into mature minibasins (e.g. Fernandez and Kaus, 2015). Thus, any differences between the simulations regarding size, geometry and spacing of minibasins is exclusively due to differences in the parameters used for the sediment properties. Cohesion and friction angle determine the effective strength of the minibasins, resulting in relatively weak (i.e. low cohesion and friction angle) or relatively strong (i.e. high cohesion and friction angle) minibasins. The effective strength of a minibasin affects its overall subsidence history and thus the contained stratal pattern.

During the numerical simulations, the velocity field obtained for each time step is used to extract the X and Z velocity components across the model domain. X and Z velocity components are then averaged per model domain column (in Z dimension) for the salt and for the sediments separately. The results show the variation of the mean X and Z velocity of salt and sediments across the model length (in X dimension). Positive value of X component of velocity indicate a flow towards the right, whereas negative values, indicate flow in the opposite direction. Positive values of Z component of velocity indicate an upward flow, whereas negative values indicate downward directed flow.

Modeling Results

In this section we describe three different simulations to illustrate the evolution of minibasins formed by density-driven subsidence in the models. Simulation 1 shows the evolution of one single isolated minibasin that formed from a pre-kinematic seed. Simulations 2 and 3 are two examples where no pre-kinematic seeds were used and where arrays of minibasins formed spontaneously across the model. The specific physical parameters of the three simulations are given in Table 2.

Isolated minibasin sinking into thick salt

In simulation 1, an initial pre-kinematic layer of sediments was added in the setup. This layer is 1 km long and 200 m thick, with a thicker (400 m-thick) central segment (Figs. 4A, 5A). As sediments are denser than salt in the models, the pre-kinematic layer subsides into the salt as soon as the simulation starts. Density-driven subsidence of the pre-kinematic layer creates accommodation, so sediment deposition is concentrated above the seed, forming a minibasin that is thickest at the center (Fig. 5A). As the minibasin becomes thicker and, thus, more difficult to deform in the center, bending of the flanks is limited to very narrow areas closest to the salt (cf. halokinetic folds of Giles and Lawton, 2002, Giles and Rowan, 2012). The minibasin is initially widening as it subsides, until it starts narrowing upwards (after time ~ 1.56 Myrs, Fig. 5A). Overall, the isolated minibasin of simulation 1 subsides symmetrically throughout its history, with this being recorded by symmetric stratal geometries within the minibasin (Fig. 5A).

The mean X and Z velocity components of simulation 1 are shown in Fig. 5B. The X component of the mean salt velocity shows a positive peak to the right side of the minibasin, and a negative peak to the left side of the minibasin (Fig. 5B). The two mean salt velocity peaks of the X components are of equal magnitude ($Vx_{max} = -Vx_{min}$) (Fig. 5B). Away from the minibasin, the mean X component salt velocity decreases gradually towards zero. The Z component of the mean salt velocity has the highest negative value below the center of the minibasin (Vz_{mean}) and two positive and equal value mean-velocity peaks to either side of the minibasin ($Vz_{lpeak} = Vz_{rpeak}$) (Fig. 5B, red). Away from the minibasin, the mean Z salt velocity decreases rapidly towards zero (Fig. 5B) As the isolated minibasin continues to subside into thick salt and becomes thicker, more salt is evacuated from below the minibasin, thus the magnitude of the mean X salt velocity peaks increase until the minibasin welds at the base (Fig. 5B). Overall, salt velocity components indicate that salt is expelled from below the subsiding minibasin to both sides equally, feeding flanking diapirs that rise at similar rates. The generalized plot of the mean salt velocities for an isolated minibasin subsiding into thick salt is shown in Fig. 5C.

The velocity field within the sediments is simpler, with the predominant Z component of the velocity illustrating the subsidence of the minibasin as a downward directed symmetric flow (Fig. 5B). Interestingly, when the minibasin is thin and weak enough to be able to accommodate deformation, the velocity in Z direction shows a maximum value in the center of the minibasin decreasing toward the flanks; this suggests deformation by folding. As the minibasin becomes thicker and stronger, the Z velocity shows a constant value across the width of the minibasin, indicating no internal deformation (i.e. folding). In both cases, the plots are symmetric.

The evolution of the sediment accumulation rate through time is shown in Fig. 5D. At the very early stages, the sediment accumulation rate increases very fast, until it reaches a maximum of 0.05 cm/year. Afterwards, sediment accumulation rate decreases steadily until the minibasin welds (at time ~ 4.00 Myrs). After welding, sediment accumulation rate of the minibasin corresponds to the imposed aggradation rate of 0.002 cm/year.

Minibasin arrays sinking into thick salt

Having investigated how a single isolated minibasin subsides in simulation 1, we now explore the evolution of minibasin arrays in simulations 2 and 3 (Fig. 6). These two simulations differ only in the properties used to model the sediments (C and Φ, Table 2). Minibasin initiation process and overall minibasin evolution is similar in both simulations, so both models are described together. The simulations start with a flat layer of salt without a capping pre-kinematic sediment layer (Fig. 4B). Once the simulation begins, the first sediment layer deposited is very thin, and not completely uniform in thickness due to the random noise used to perturb the position of the markers. This tiny variation in the thickness of the early sediment load produces differential subsidence into the salt and the formation of individualized thin minibasins (Fig. 6 A, B; time ~1.96 m.y.). It must be emphasized that the initial layers of sediments are thin compared to subsequent ones, because at this early stage, the subsidence into salt is minimal. As the minibasins subside into the salt, accommodation for new sediments is created on top of them, and the initially thin minibasins eventually evolve into thicker and wider minibasins (Fig. 6 A, B; time ~1.96 m.y. and onwards). The minibasins formed in the two simulations are numbered 1-13 (Fig. 6). In each simulation 6 to 10 minibasins form ranging in width and thickness (Fig. 6). A striking characteristic of these simulations is that minibasins initiate asynchronously. Initially, thin sediment pods are roughly regularly spaced across the model, but a few of them start subsiding faster than others (e.g. minibasins 3, 7, 10 and 13; Fig. 6). As a result, at any given time, minibasins of different thicknesses are subsiding at different rates. This asynchronous subsidence is also reflected in the sediment accumulation rates in the minibasins shown in Fig. 7, where each minibasin reaches a peak sediment accumulation rate at a different time. The minibasins that subside fastest weld to the base of salt before the slower-subsiding minibasins. Once the first minibasins (e.g. minibasins 3, 7, 10 and 13) weld, other minibasins (e.g. minibasins 1, 4, 6, 11 and 12) subside more quickly (Fig. 6). The process of minibasin formation described above results in varied stratigraphic patterns within the minibasins. While some minibasins are symmetric in cross section, many others exhibit very asymmetric geometries because of their complex subsidence histories. Next, we will look in more detail at various examples of minibasin to illustrate stratigraphic geometries.

Symmetric minibasins

Symmetric minibasins having continuous subsidence

Minibasin 3 (Fig. 6A) is an example of a minibasin that records symmetric subsidence throughout its evolution, resulting in symmetric sediment fill composed of a basal symmetric bowl and overlying layers (Fig. 8A). Minibasin 3 is also one of the depocenters that undergoes initially rapid subsidence and increased sediment accumulation rates (Fig. 7A). Minibasin 3 initiates with a bowl-shaped geometry (e.g. Fig. 8A), indicating a higher rate of subsidence in the center. Minibasin 3 welds to the base of salt at around time: ~2.96 m.y. and therefore cannot subside vertically anymore (Fig. 6A). However, due to the fact that the overall salt level is rising in the simulation (by evacuation of salt from beneath surrounding minibasins), accommodation is still generated above the now-welded minibasin 3 (post-weld layer, Fig. 8A). After its welding, sediment accumulation in minibasin 3 is only occurring due to the background sediment aggradation and thus, the sediment accumulation rate of minibasin 3 corresponds to the imposed aggradation rate at this stage (Fig. 7A). As accommodation is created only by aggradation at this stage, layers deposited after welding are thinner than during the preceding phase of vertical subsidence into thick salt (Figs. 6A and 8A, time ~ 3.96 m.y. and onwards). Furthermore, the minibasin narrows-upwards at this stage, which indicates that salt inflation, driven by continued subsidence of other minibasins in the array, is faster than sediment aggradation (Fig. 8A).

Other minibasins also display symmetric geometries (6, 10, and 13; Figs. 6 and 8). Minibasins 10 and 13 in simulation 3 (Fig. 6B) are adjacent, thus, we examine their velocity profiles together (Fig. 9). At an early stage (Fig. 9A), subsidence of minibasins 10 and 13 is clearly visible in the mean Z sediment velocity plot (marked with "S" in Fig. 9A). Also, their sediment accumulation rate reaches their peak value before any of the other minibasins in simulation 3 (Fig. 7B). The horizontal and vertical flow of salt around minibasins 10 and 13 is visible in the mean salt velocity plots as more complex variations in amplitude (Fig. 9A). However, the mean salt velocity profiles of minibasins 10 and 13 are very similar to the velocity profile of a single isolated minibasin (cf. Figs. 5 and 9). As minibasins 10 and 13 continue to subside, horizontal (X) and vertical (Z) salt flow velocities increase until welding, when they decrease again (Fig. 9). After their welding, sediment accumulation rate corresponds to the aggradation rate imposed in the models (Fig. 7B). Minibasins 10 and 13 initiate first in simulation 3, so they subside into a fairly unperturbed salt layer. Furthermore, they are far enough from each other so that their velocity perturbations do not overlap or affect each other.

Symmetric minibasins having discontinuous subsidence

Minibasins 9 and 12 also initiate early in simulation 3, at which time they develop symmetrical geometries formed in response to early symmetric subsidence into thick salt (Fig. 6B and 9B). Early subsidence of minibasin 12 is observed in the velocity plot as a characteristic mean sediment Z velocity signature defined as a small downwards undulation (marked "S" in Fig. 9B). However, as denoted by the absence of the same characteristic velocity signal in Fig. 9C, at time ~3.46 m.y., minibasin 12 is not subsiding. By time ~4.76 m.y., minibasin 12 is again subsiding as indicated by the strong downward undulation in Z velocity plot (marked "S", Fig. 9D). We interpret that subsidence of minibasin 12 was interrupted by a short period of no subsidence (Fig. 9C) before resuming rapid subsidence later in the simulation (Fig. 9D). This discontinues subsidence is reflected in the lack of sediment accumulation (accumulation rate equals zero) in minibasins 9 and 12 for a period time (Fig. 7B). Why should this be so? To begin, the mean salt velocity signal beneath the early-formed minibasin 12 is small compared to nearby minibasins 11 and 13, which are subsiding more rapidly during this early phase (Fig. 9B). Later, the strong velocity perturbation generated by rapid subsidence of minibasin 11 extends across minibasin 12, completely overprinting the (X and Z) velocity signal of minibasin 12 (Fig. 9C). The lateral and upward flow of salt from beneath minibasin 11 towards minibasin 12 prevents minibasin 12 from subsiding. Instead, minibasin 12 moves laterally (compare Fig. 9C and D). Minibasin 12 resumes its subsidence when minibasin 11 approaches the base of salt, and the rate of expulsion of salt from beneath it decreases (Fig. 9D). At that stage, minibasin 12 resumes its symmetric subsidence into a relatively quiescent salt compartmentalized in between two welded minibasins. Velocity profiles of minibasin 12 at this stage are similar to the profiles of single isolated minibasins (compare Fig. 5 and 9D). We conclude that subsidence of minibasins can inhibit subsidence of another minibasin.

Asymmetric minibasins

Abrupt shifts of depocenters, where minibasins transition from a symmetric basal bowl-shaped to an asymmetric wedge-shaped geometry, have been observed in the Gulf of Mexico (Rowan and Weimer, 1998), Precaspian Basin (Jackson et al., 2019) and in other salt basins (e.g. Sivas Basin; Kergaravat et al., 2016). The bowl-to-wedge transitions observed in some minibasins of the Gulf of Mexico had been interpreted as being the result of minibasin welding and subsequent lateral collapse (Rowan and Weimer, 1998). However, other mechanisms (e.g., syn-subsidence shortening, salt emplacement on top of minibasin) may trigger tilting prior to welding (e.g. Hudec, 2009; Jackson et al., 2019).

Our models show minibasin tilting both before and after welding. About half of the minibasins in Fig. 6 are symmetric, but the others show significant degrees of asymmetry, as indicated by sediment fill that thickens towards one side of the minibasin. Several of the minibasins in our models begin tilting prior to welding (e.g., minibasins 4 and 11, Fig. 8C-D). Others show tilting only after welding, and still others show tilting both before and after (sometimes in opposite directions; e.g. minibasin 4, Fig. 4D). In this section we discuss the origin of minibasin tilting both before and after welding, along with controls on the direction and timing of tilt.

Minibasin tilting prior to basal welding

Minibasins 11 and 4 initiate as bowl-shaped minibasins, recording a period of symmetric subsidence (Fig. 8C-D). On top of the symmetric bowl sequences, wedge-shaped sequences form due to tilting and asymmetric subsidence. This initial tilting occurs prior to welding, and in both cases the tilt is away from the nearest actively subsiding minibasin (Fig. 8C-D).

Minibasin 11 initiates relatively early in the simulation, at a time when the minibasin immediately to its left, minibasin 10, is already subsiding rapidly (Fig. 8C, 9A and B). On its right side, by contrast, minibasin 12 is much thinner and has a slower subsidence, which eventually stops at a later stage (cf. Fig. 9B, C). Even further to the right, minibasin 13 is nearly welded by the time minibasin 11 starts its main phase of subsidence, so minibasin 13 is not expelling much salt (Fig. 9C). Thus, during its main phase of subsidence, salt flow around minibasin 11 is asymmetric, most heavily influenced by expulsion of salt from beneath minibasin 10 (Fig. 9B-C). In fact, the mean salt velocity signal around minibasin 11 shows that the peak of Vx_{11max} (positive value), is more prominent than the low Vx_{11min} (negative value) (Fig. 9B). As a result of this asymmetric salt flow around it, minibasin 11 starts subsiding asymmetrically (mean sediment velocity marked with "A" in Fig. 9C), tilting towards the direction in which the salt flow has been increased (to the right). Once minibasin 10 is welded and the associated salt flow stops (Fig. 9C), minibasin 11 resumes a purely symmetric subsidence, recorded by a constant-thickness sedimentary layer deposited just before welding (t=3.96 Myrs, Fig. 8C).

Other minibasins showing pre-welding asymmetric subsidence (e.g., minibasin 5, Fig. 8D), can also be explained by appealing to tilting away from the nearest actively subsiding minibasin. Thus, we conclude that tilting before welding of a minibasin can be induced by nearby minibasin subsidence and the resulting alteration of salt-flow patterns.

Minibasin tilting after basal welding

Tilting of minibasins also occurs in the simulations after basal welding. For example, the upper, strongly wedge-shaped sequences of minibasins 4, 7, and 11 all form late, after the minibasins weld (e.g. Fig. 6 and 8B to C). Focusing again on minibasin 11, this minibasin welds at its base after a complex history of tilting followed by a late stage of symmetric subsidence (Figs. 8C and 9D). When minibasin 11 welds, minibasin 10 to its left is already welded, but minibasin 12 to its right starts subsiding more rapidly (Fig. 9D). Accelerated symmetric subsidence of minibasin 12 is reflected in the strong and symmetric velocity signal visible in the X velocity component of the mean salt velocity plot (Fig. 9D). Expulsion of salt from below minibasin 12 into the diapir between minibasins 11 and 12 induces pivoting of minibasin 11 away from the inflating salt structure (Fig. 9D).

From this we conclude that once minibasins (symmetric or asymmetric) weld at their base, their subsequent evolution (tilting vs symmetrical aggradation) depends not only on whether there are nearby actively subsiding minibasins that can induce salt inflation and subsequent tilting, but also on the minibasin basal geometry. Minibasin geometry affects the potential for the minibasin to pivot around the weld contact point (e.g. Callot et al., 2016). We suggest that broadly symmetric minibasins with a centered basal weld contact point are potentially more stable and able to resist tilting even in the presence of nearby subsiding minibasins (e.g. minibasin 10, Fig. 6B). In contrast, minibasin with an off-centered basal weld contact point (asymmetric minibasins), will more easily pivot and tilt (e.g. minibasin 4 and 11, Fig. 6).

Discussion

'Competition' for salt between minibasins subsiding at different rates

In our single-minibasin numerical simulations, minibasins subside symmetrically (e.g., Fig. 5). Tilting before welding only occurs in our simulations with multiple minibasins, suggesting that the presence of multiple minibasins subsiding at different rates facilitates the formation of asymmetric minibasins. In the numerical models by Gradmann and Beaumont (2017), asymmetric minibasins are formed as a result of sustained and localized sedimentation with a pre-stablished optimal wavelength (Goteti et al., 2012). In the absence of shortening, the rotation and tilting of the minibasins that form synchronously in the simulations might be related to the containment of the salt basin and the presence of a directional salt flow towards the basin center (Gradman and Beaumont, 2017). In the numerical simulations presented here, minibasins subside at different rates (asynchronously) and there is slope that would promote an additional lateral component of salt flow. If minibasin subsidence is purely density-driven, thicker and bigger minibasins subside faster and thus displace salt at higher rates than smaller and thinner minibasins. The salt being expelled from below each subsiding minibasin moves into the surrounding salt structures (typically diapirs; Fig. 9). If several minibasins are subsiding simultaneously, a complex salt flow will result from the combination of all the individual velocity perturbations. Bigger velocity perturbations induced by bigger minibasins will overprint the smaller velocity perturbations of smaller minibasins. Overall, subsiding minibasins affect each other's subsidence histories through the velocity perturbations they induce in the salt flowing around them. We thus propose that minibasins, even if not in contact or connected by a roof, are kinematically interacting, so that subsidence history of each minibasin cannot be understood without looking at the subsidence history of the surrounding minibasins.

Minibasin interaction styles and implications

Based on observations from our numerical models, we propose that interactions between adjacent minibasins that are not in contact with each other can occur. However, we also found that some minibasins within the arrays do not interact with other minibasins. The simplest possible scenario for lack of minibasin interactions is the case in which a minibasin forms in isolation and subsides vertically thorough its evolution resulting in purely symmetrical stratigraphic geometries (e.g. simulation 1, Fig. 5). Minibasins rarely form in complete isolation in nature and are invariable part of broader minibasin arrays. However, within minibasin arrays, a minibasin can also subside without interacting with adjacent minibasins if there are no minibasins sinking nearby (minibasins 3, 10, and 12; Fig. 6). There are two factors that can influence if minibasins within the array will interact. The first factor to consider is the timing of minibasin subsidence. Some of the symmetric minibasins observed in our simulations are the ones that subside early in the simulations, when other minibasins have not yet formed, and so, are effectively subsiding in isolation (e.g., minibasins 3 and 10, Fig. 6). In this regards, observations from the Green Canyon area in the deep-water Gulf of Mexico support this scenario, since one of the minibasins that subsided earlier (Miocene) into a thick salt canopy displays simple symmetric geometries as compared to the later subsiding minibasins (Pliocene) that were formed coevally in between other minibasins (Moore and Hinton, 2013). Some other minibasins in our simulations subside later within minibasin arrays and yet, also display overall symmetric geometries. Late-subsiding minibasins may do so, after adjacent minibasins have grounded and thus are not expelling any salt. As a result, these late-subsiding minibasins sink into a relatively unperturbed salt in between grounded minibasins, and can subside symmetrically developing symmetric stratigraphic geometries. Effectively, these late-subsiding minibasins are also not being affected by any salt flow perturbation induced by nearby subsiding minibasins. The second factor that can explain the lack of interactions within arrays of minibasins is the spacing or distance between subsiding minibasins. A minibasin subsiding within an array may be far enough from the closest actively subsiding minibasin so that it is not affected by the associated salt flow perturbations.

Having outlined the scenarios in which minibasins may not interact with other minibasins of the array, we next discuss the cases in which minibasin do interact. As pointed out before, adjacent subsiding minibasins can interact if they are close enough to affect each other. In our simulations, we have observed numerous styles of minibasin interactions. While some interactions result in asymmetric stratal geometries of the minibasins, other interactions do not necessarily result in asymmetric geometries.

In our simulations, we have observed two interaction styles that do not necessarily result in asymmetric geometries of the minibasins. First, actively subsiding thick minibasins can prevent other nearby thinner minibasins from subsiding (e.g., minibasins 6 and 12; Fig. 10B). Once the actively subsiding minibasins are grounded, the minibasin whose subsidence was prevented, can resume its symmetric subsidence again (Fig. 10B). An important implication of discontinued subsidence is that minibasins can have incomplete stratigraphic sections, with hiatuses representing the time when subsidence was not occurring even if the depositional systems feeding them were still active (Fig. 10B and C). Second, actively subsiding minibasins can induce the lateral translation of a thinner nearby minibasin (Fig. 10C, E). In fact, many of the minibasins in the simulations of minibasin arrays display a certain amount of lateral translation (indicated by the arrows in minibasins 4, 6, 11 and 12 of Fig. 6). Each arrow indicates the distance between the initial and final position of the depocenter during the simulation. Translation occurs wherever there is an asymmetry in horizontal flow on either side of a minibasin (e.g., minibasin 12 in Fig. 9). Thicker and more massive minibasins are more difficult to translate, and we do not see translation in our models after basal welding. As in the case of minibasins with discontinued subsidence, minibasins that are laterally translated, may also have an incomplete stratigraphic sequence.

Another style of minibasin interaction is one that can lead to the formation of asymmetric minibasins before basal welding occurs (Fig. 10D). If subsidence of nearby minibasins results in an asymmetric salt flow around a minibasin, salt from below the minibasin is evacuated preferentially towards one side. This scenario results in the tilting of the minibasin towards the side of preferential evacuation, as recorded by thickening of the sedimentary sequence that is being deposited on top of the asymmetrically subsiding minibasin. For example, minibasins 4 and 11 tilted before basal welding (Fig. 6, 8, 9). The observation that minibasins can tilt before basal welding has important implications for interpreting weld timing. The bowl-to-wedge transitions in the stratal geometries of minibasins has previously been linked to the basal welding of minibasins (Rowan and Weimer, 1998). Our numerical models illustrate that this interpretation may not be appropriate in all cases, as pre-welding tilting of minibasins can occur due to the kinematic interactions between minibasins (see also Jackson et al., 2019).

Finally, as observed in our models, minibasin interactions can also induce tilting of a grounded minibasin (Fig. 10F). Once a minibasin is grounded, the salt displaced by an adjacent subsiding minibasin can cause the grounded minibasin to tilt away from the inflating salt structure (e.g. Minibasin 7; Fig. 6A). After welding, subsidence of minibasin 8 to the right induced the tilting away of minibasin 7 to the left (Fig. 6A). Tilting of asymmetric minibasins after welding is also common in the simulations. In some cases, the tilt direction reverses after welding (e.g. minibasins 4 and 11, Fig. 6, 8 and 9), resulting in the stacking of wedge-shape sequences that thicken in opposite directions.

Although our models have addressed the interactions between minibasins from a two-dimensional perspective, salt flow is a very three-dimensional process. In contrast to our models, in a three-dimensional framework, salt can be expelled in any direction within the salt volume, across salt walls and diapirs surrounding the minibasins. On the one hand, because salt may spread in more directions, it is likely that the interactions among nearby minibasins described here (e.g. discontinued subsidence and tilting) would be mitigated. On the other hand, it means that there is more potential for differential salt flows in the horizontal plane; this could cause minibasin rotation about a sub-vertical axis as observed in physical models where minibasins collide (e.g. Rowan and Vendeville, 2006; Callot et al., 2016).

Conclusions

Two-dimensional numerical models were performed to study a scenario in which minibasins were initiated and subsided into salt at different rates, without slope-driven regional salt flow or tectonic deformation. The goal of the study was to test the hypothesis that minibasins are able to interact through the complex patterns of salt flow that results when adjacent minibasins are subsiding at different rates (e.g. Jackson et al., 2019). Our models show that minibasins do indeed interact, and that minibasins may tilt, translate, or experience delays in subsidence due to subsidence of nearby minibasins. These interactions are all results of a competition between subsiding minibasins for the finite available salt volume. Ultimately, the complex subsidence history is reflected in the complex patterns of minibasin sedimentation.

Minibasin interpretation usually assumes either vertical density-driven subsidence, or subsidence dominated by a regional salt flow. Regional salt flow can indeed be important, especially in areas where large-scale basinward movement of salt has been identified or where the basin experiences regional tectonics. However, minibasins do not necessary have undergone a simple history of purely vertical subsidence in tectonically quieter areas. Locally induced perturbations to the salt flow can be caused by the differential rates of salt expulsion related to the different subsidence rates of minibasins. The interactions illustrated by the numerical models shown in this study suggest that minibasin subsidence occurs in a dynamic system in which minibasins do not act as mere recorders of the salt flow around them, but rather they are also the drivers that can influence and alter that salt flow by themselves.

We suggest that interactions between adjacent minibasins that have not collided should be considered when interpreting stratal patterns within minibasins, particularly in areas where the salt-tectonic processes are thought to be purely vertical. The models shown in this work illustrate that even in such areas, minibasins can have complex subsidence histories due to interactions between them.

Acknowledgements

Boris Kaus is specially acknowledged for developing and making available the numerical code MVEP2. MVEP2 can be downloaded at https://bitbucket.org/bkaus/mvep2/. We are also grateful to the reviewers Chris Beaumont and Zhiyuan Ge who provided useful comments that helped improving the manuscript. We thank Nancy Cottington for her help with figure drafting. This project was funded by the Applied Geodynamics Laboratory (AGL) Industrial Associates program, comprising the following companies: Anadarko, Aramco Services, BHP Billiton, BP, CGG, Chevron, Condor, EcoPetrol, EMGS, ENI, ExxonMobil, Hess, Ion-GXT, Midland Valley, Murphy, Nexen USA, Noble, Petrobras, Petronas, PGS, Repsol, Rockfield, Shell, Spectrum, Equinor, Stone Energy, TGS, Total, WesternGeco, and Woodside (http://www.beg.utexas.edu/agl/sponsors). The authors received additional support from the Jackson School of Geosciences, The University of Texas at Austin.

References

Banham, S. G., and Mountney, N. P., 2013, Evolution of fluvial systems in salt-walled mini-basins: A review and new insights: Sedimentary Geology, v. 296, p. 142-166.

Barde, J.-P., Chamberlain, P., Galavazi, M., Gralla, P., Harwijanto, J., Marsky, J., and van den Belt, F., 2002, Sedimentation during halokinesis: Permo-Triassic reservoirs of the Saigak Field, Precaspian Basin, Kazakhstan: Petroleum Geoscience, v. 8, no. 2, p. 177-187.

Barde, J.-P., Gralla, P., Harwijanto, J., and Marsky, J., 2002b, Exploration at the Eastern Edge of the Precaspian Basin: Impact of Data Integration on Upper Permian and Triassic Prospectivity: AAPG Bulletin, v. 86, no. 3, p. 399-415.

Biot, M., and Odé, H., 1965, Theory of gravity instability with variable overburden and compaction: Geophysics, v. 30, no. 2, p. 213-227.

Callot, J.-P., Ribes, C., Kergaravat, C., Bonnel, C., Temiz, H., Poisson, A., Vrielynck, B., Salel, J.-F., and Ringenbach, J.-C., 2014, Salt tectonics in the Sivas basin (Turkey): crossing salt walls and minibasins: Bulletin de la Societe Geologique de France, v. 185, no. 1, p. 33-42.

Callot, J.-P., Salel, J.-F., Letouzey, J., Daniel, J.-M., and Ringenbach, J.-C., 2016, Three-dimensional evolution of salt-controlled minibasins: Interactions, folding, and megaflap development: AAPG Bulletin, v. 100, no. 9, p. 1419-1442.

Crameri, F., Schmeling, H., Golabek, G. J., Duretz, T., Orendt, R., Buiter, S. J. H., May, D. A., Kaus, B. J. P., Gerya, T. V., and Tackley, P. J., 2012, A comparison of numerical surface topography calculations in geodynamic modelling: an evaluation of the 'sticky air' method: Geophysical Journal International, v. 189, no. 1, p. 38-54.

Dabrowski, M., Krotkiewski, M., and Schmid, D. W., 2008, MILAMIN: MATLAB-based finite element method solver for large problems: Geochemistry, Geophysics, Geosystems, v. 9, no. 4, p. Q04030.

Duffy, O. B., Fernandez, N., Hudec, M. R., Jackson, M. P. A., Burg, G., Dooley, T. P., and Jackson, C. A. L., 2017, Lateral mobility of minibasins during shortening: Insights from the SE Precaspian Basin, Kazakhstan: Journal of Structural Geology, v. 97, p. 257-276.

Fernandez, N., Duffy, O. B., Hudec, M. R., Jackson, M. P. A., Burg, G., Jackson, C. A. L., and Dooley, T. P., 2017, The origin of salt-encased sediment packages: Observations from the SE Precaspian Basin (Kazakhstan): Journal of Structural Geology, v. 97, p. 237-256.

Fernandez, N., and Kaus, B. J. P., 2015, Pattern formation in 3-D numerical models of down-built diapirs initiated by a Rayleigh–Taylor instability: Geophysical Journal International, v. 202, no. 2, p. 1253-1270.

Fiduk, J. C., and Rowan, M. G., 2012, Analysis of folding and deformation within layered evaporites in Blocks BM-S-8 & -9, Santos Basin, Brazil: Geological Society, London, Special Publications, v. 363, no. 1, p. 471-487.

Giles, K. A., and Lawton, T. F., 2002, Halokinetic Sequence Stratigraphy Adjacent to the El Papalote Diapir, Northeastern Mexico: AAPG Bulletin, v. 86, no. 5, p. 823-840.Giles, K. A., and Rowan, M. G., 2012, Concepts in halokinetic-sequence deformation and stratigraphy: Geological Society, London, Special Publications, v. 363, no. 1, p. 7-31.

Goteti, R., Ings, S. J., and Beaumont, C., 2012, Development of salt minibasins initiated by sedimentary topographic relief: Earth and Planetary Science Letters, v. 339–340, no. 0, p. 103-116.Gradmann, S., and Beaumont, C., 2017, Numerical modelling study of mechanisms of mid-basin salt canopy evolution and their potential applications to the Northwestern Gulf of Mexico: Basin Research, v. 29, no. 4, p. 490-520.

Hudec, M. R., and Jackson, M. P. A., 2007, Terra infirma: Understanding salt tectonics: Earth-Science Reviews, v. 82, no. 1–2, p. 1-28.

Hudec, M. R., Jackson, M. P. A., and Schultz-Ela, D. D., 2009, The paradox of minibasin subsidence into salt: Clues to the evolution of crustal basins: Geological Society of America Bulletin, v. 121, no. 1-2, p. 201-221.

Jackson, M. P. A., and Hudec, M. R., 2017, Salt Tectonics: Principles and Practice, Cambridge, Cambridge University Press.

Jackson, C. A. L., Duffy, O. B., Fernandez, N., Dooley, T., Hudec, M., Jackson, M., & Burg, G. (2019). The Stratigraphic Record of Minibasin Subsidence. PREPRINT

Johnson, T. E., Brown, M., Kaus, B. J. P., and VanTongeren, J. A., 2013, Delamination and recycling of Archaean crust caused by gravitational instabilities: Nature Geoscience, v. 7, p. 47.

Kaus, B. J. P., 2010, Factors that control the angle of shear bands in geodynamic numerical models of brittle deformation: Tectonophysics, v. 484, no. 1–4, p. 36-47.

Kergaravat, C., Ribes, C., Legeay, E., Callot, J.-P., Kavak, K. S., and Ringenbach, J.-C., 2016, Minibasins and salt canopy in foreland fold-and-thrust belts: The central Sivas Basin, Turkey: Tectonics, v. 35, no. 6, p. 1342-1366.

Koyi, H., 1998, The shaping of salt diapirs: Journal of Structural Geology, v. 20, no. 4, p. 321-338.

Matthews, W. J., Hampson, G. J., Trudgill, B. D., and Underhill, J. R., 2007, Controls on fluviolacustrine reservoir distribution and architecture in passive salt-diapir provinces: Insights from outcrop analogs: AAPG Bulletin, v. 91, no. 10, p. 1367-1403.

Moore, V. and Hinton, D., 2013, Secondary basins and sediment pathways in Green Canyon, deepwater Gulf of Mexico AAPG Search and Discovery Article, AAPG Annual Convention and Exhibition, Pittsburgh, USA (2013)

Mukherjee, S., Talbot, C. J., and Koyi, H. A., 2010, Viscosity estimates of salt in the Hormuz and Namakdan salt diapirs, Persian Gulf: Geological Magazine, v. 147, no. 04, p. 497-507.

Pichat, A., Hoareau, G., Callot, J.-P., and Ringenbach, J.-C., 2019, Characterization of Oligo-Miocene evaporite-rich minibasins in the Sivas Basin, Turkey: Marine and Petroleum Geology, v. 110, p. 587-605.

Prather, B. E., 2003, Controls on reservoir distribution, architecture and stratigraphic trapping in slope settings: Marine and Petroleum Geology, v. 20, no. 6, p. 529-545.

Prochnow, S. J., Atchley, S. C., Boucher, T. E., Nord, L. C., and Hudec, M. R., 2006, The influence of salt withdrawal subsidence on palaeosol maturity and cyclic fluvial deposition in the Upper Triassic Chinle Formation: Castle Valley, Utah: Sedimentology, v. 53, no. 6, p. 1319-1345.

Rowan, M. G., and Weimer, P., 1998, Salt-sediment interaction, northern Green Canyon and Ewing Bank (offshore Louisiana), northern Gulf of Mexico: AAPG Bulletin, v. 82, no. 5B, p. 1055-1082.

Rowan, M. G., and Vendeville, B. C., 2006, Foldbelts with early salt withdrawal and diapirism: Physical model and examples from the northern Gulf of Mexico and the Flinders Ranges, Australia: Marine and Petroleum Geology, v. 23, no. 9–10, p. 871-891.

Schuster, D. C., 1995, Deformation of Allochthonous Salt and Evolution of Related Salt-Structural Systems, Eastern Louisiana Gulf Coast Salt Tectonics: A Global Perspective, *in* Jackson, M. P. A., Roberts, D. G., and Snelson, S., eds., Volume 65, American Association of Petroleum Geologists.

Sylvester, Z., Cantelli, A., and Pirmez, C., 2015, Stratigraphic evolution of intraslope minibasins: Insights from surface-based modelStratigraphic Evolution of Intraslope Minibasins: AAPG Bulletin, v. 99, no. 6, p. 1099-1129.

Thielmann, M., and Kaus, B. J. P., 2012, Shear heating induced lithospheric-scale localization: Does it result in subduction?: Earth and Planetary Science Letters, v. 359-360, p. 1-13.

van Keken, P. E., Spiers, C. J., van den Berg, A. P., and Muyzert, E. J., 1993, The effective viscosity of rocksalt: implementation of steady-state creep laws in numerical models of salt diapirism: Tectonophysics, v. 225, no. 4, p. 457-476.

Volozh, Y., Talbot, C., and Ismail-Zadeh, A., 2003, Salt structures and hydrocarbons in the Pricaspian basin: AAPG Bulletin, v. 87, no. 2, p. 313-334.

Worrall, D. M., and Snelson, S., 1989, Evolution of the northern Gulf of Mexico, with emphasis on Cenozoic growth faulting and the role of salt: Evolution of the northern Gulf of Mexico, with emphasis on Cenozoic growth faulting and the role of salt, v. A, p. 97-138.

Table 1. Description and range of values of the physical parameters used in the simulations

Symbol	Unit	Definition	Range of values
L_x, L_z	km	Initial dimensions of model in x and z	10 to 30, 4
n_x, n_z	-	Number of nodes in x and z	100 to 300, 100
H_{salt}	km	Initial thickness of salt	1
C	MPa	Cohesion of sediments	0.0 to 3.0
ϕ	°	Friction angle of sediments	1 to 30
ρ_{sed}	kg/m^3	Density of sediments	2500 to 2650
ρ_{salt}	kg/m^3	Density of salt	2200
ρ_{air}	kg/m^3	Density of "sticky air"	0
μ_{sed}	Pa s	Viscosity of sediments	10^{25}
μ_{salt}	Pa s	Viscosity of salt	10^{18}
μ_{air}	Pa s	Viscosity of "sticky air"	10^{15}
S	cm/year	Sediment aggradation rate	0.001 to 0.01

Table 2. Specific parameters used in the simulations described in the text.

	Simulation 1: Single Minibasin	**Simulation 2: Minibasin Arrays**	**Simulation 3: Minibasin Arrays**
L_x, L_z	10 km, 4 km	30 km, 4 km	30 km, 4 km
n_x, n_z	100, 100	300, 100	300, 100
C	0.0 Mpa	0.0 Mpa	0.2 Mpa
ϕ	30°	15°	10°
S	0.002 cm/year	0.01 cm/year	0.01 cm/year

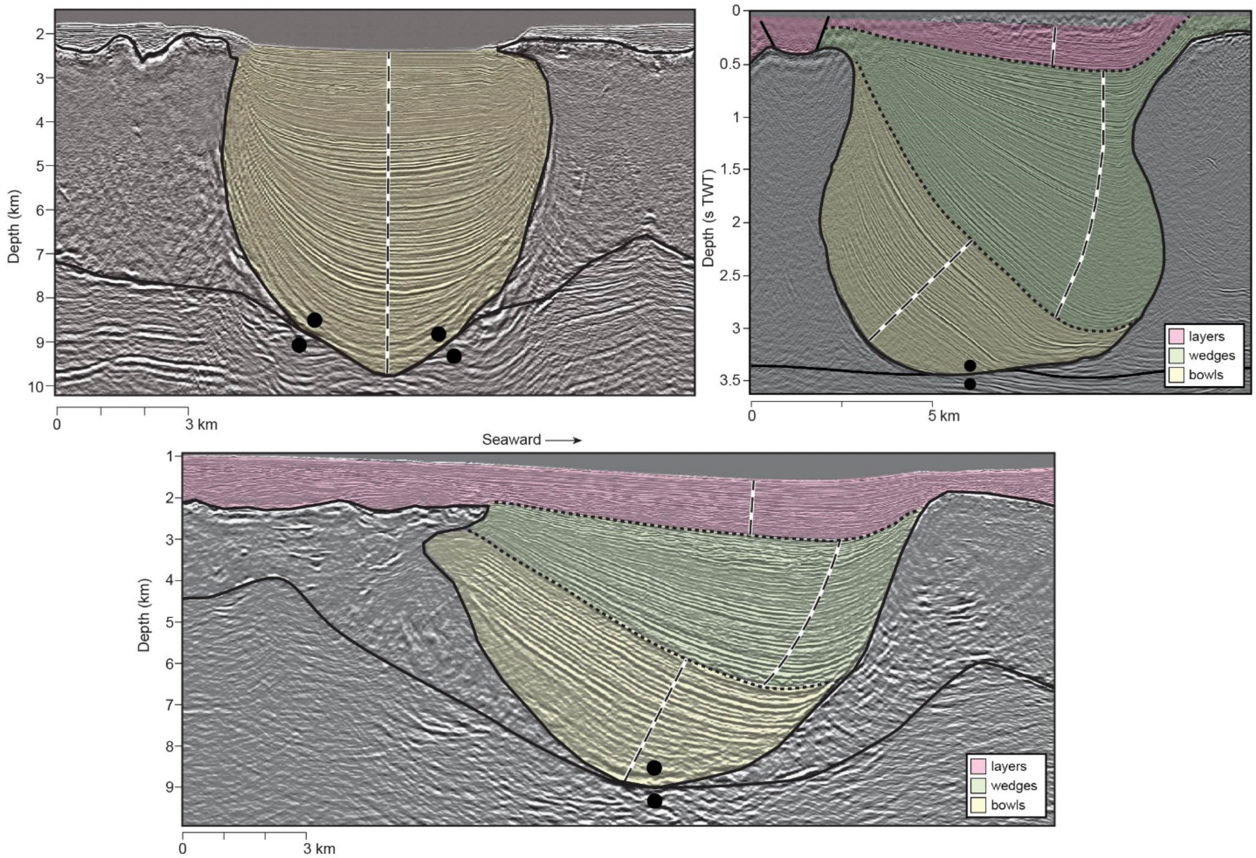

Figure 1. Seismic examples of infill patterns of minibasins. Minibasins are located in the Gulf of Mexico (A and C, modified from Hudec et al., 2009) and in the Precaspian Basin (B, modified from Jackson et al., 2019). They illustrate the variable stratal geometries that can occur, from stacked depocenters resulting in symmetric minibasin (A) to abrupt shift of depocenters, as a result of a bowl- to- wedge (sensu Rowan and Weimer, 1998) transition resulting in asymmetric minibasins (B and C) .

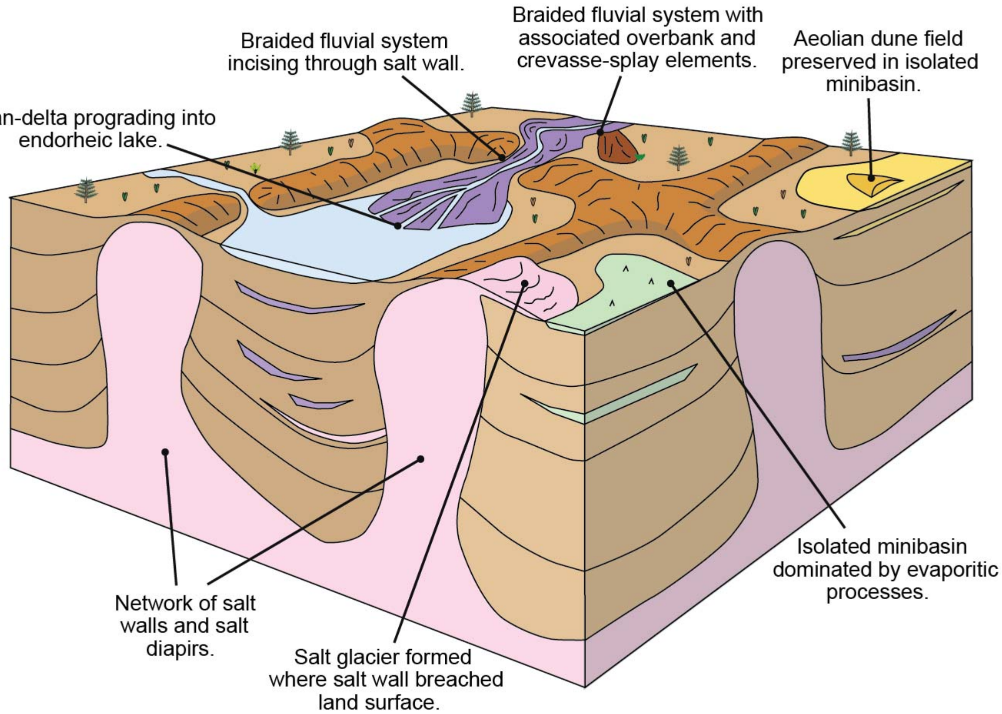

Figure 2. The basin-fill model proposed by Banham and Mountney (2013) for areas such as the Precaspian Basin, predicts that adjacent and coeval minibasins can have very different subsidence rates. The model also predicts that minibasins that are isolated from the dominant sediment transport systems within the setting, can still be infilled by the deposits resulting from: a) evaporitic dominated processes and aelian dominated processes in the case of arid climates and b) lacustrine sediments in the case of more humid climates. (Modified after Barde et al. 2002).

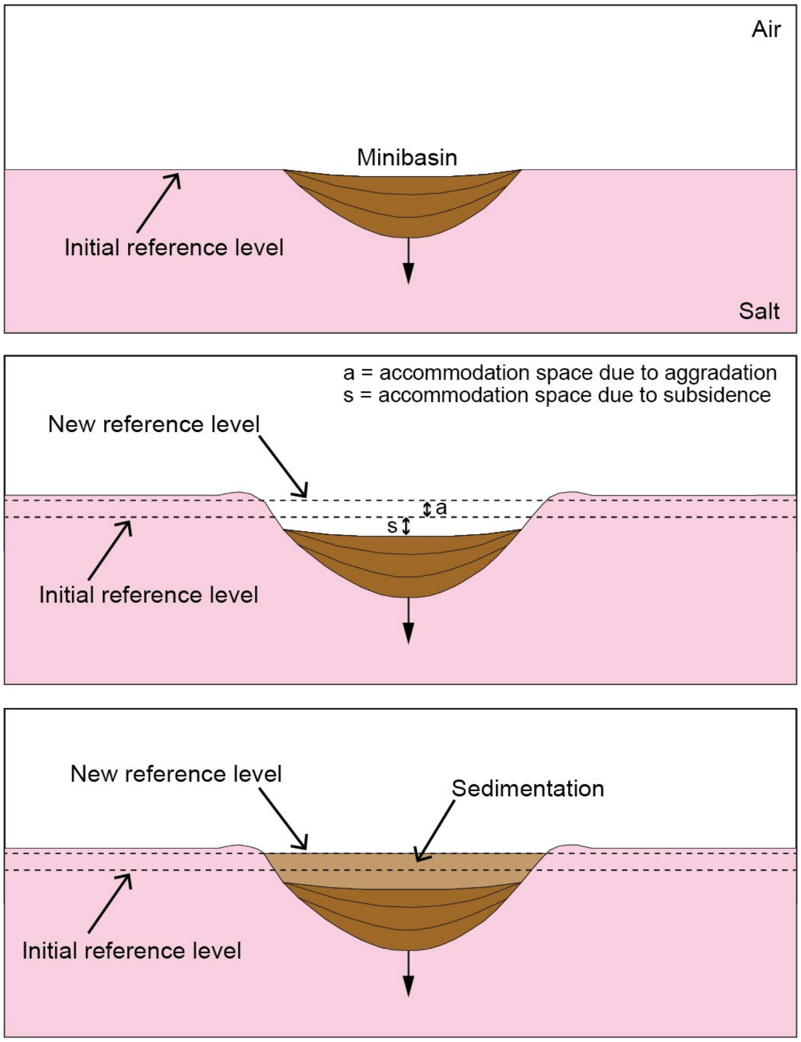

Figure 3. Schematic sketch of the implementation of the sedimentation in the numerical code. The sedimentation algorithm, uses a horizontal flat reference level that aggrades vertically according to an imposed rate. As the minibasin subsides into salt, new accommodation space is created on top of the minibasin, both due to subsidence and due to aggradation. The newly created accommodation space is filled with sediments.

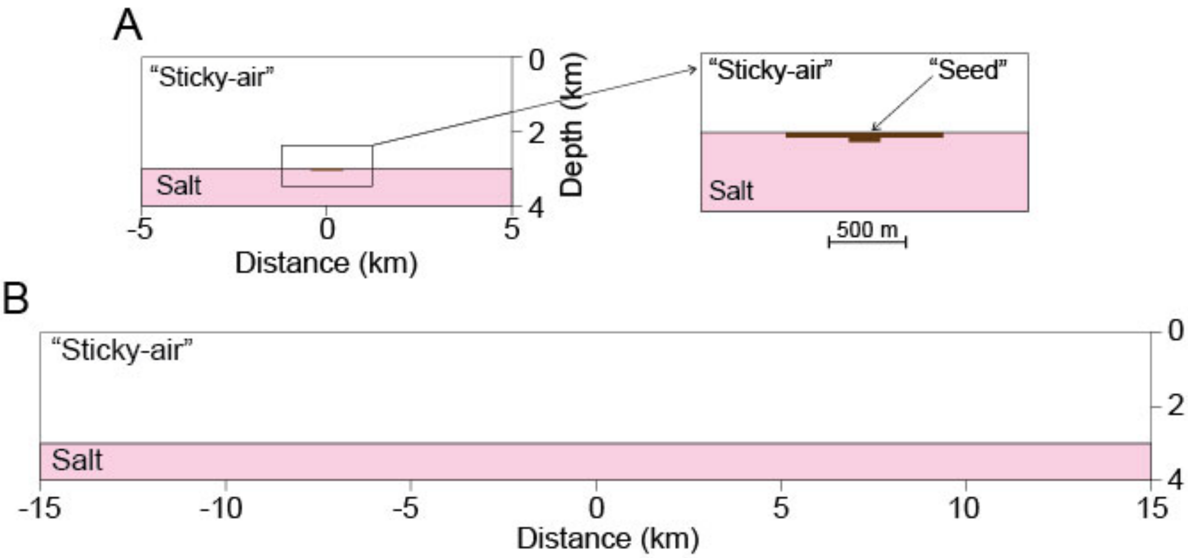

Figure 4. A. Modelling setup used for control simulations. The control setup contains a pre-kinematic sediment layer that works as a "seed" that nucleates an isolated minibasin in the center of the domain. Control simulations are aimed at illustrating the geometries of an isolated minibasin subsiding into thick salt, without any other perturbation of the salt flow. B. Modeling domain setup for the simulations with minibasin arrays discussed througout the text. There is no pre-kinematic sediment layer on top of the salt. Minibasin location is not explicitely imposed. Minibasins develop dynamically by density-driven overturn when sediments are added on top of the salt layer.

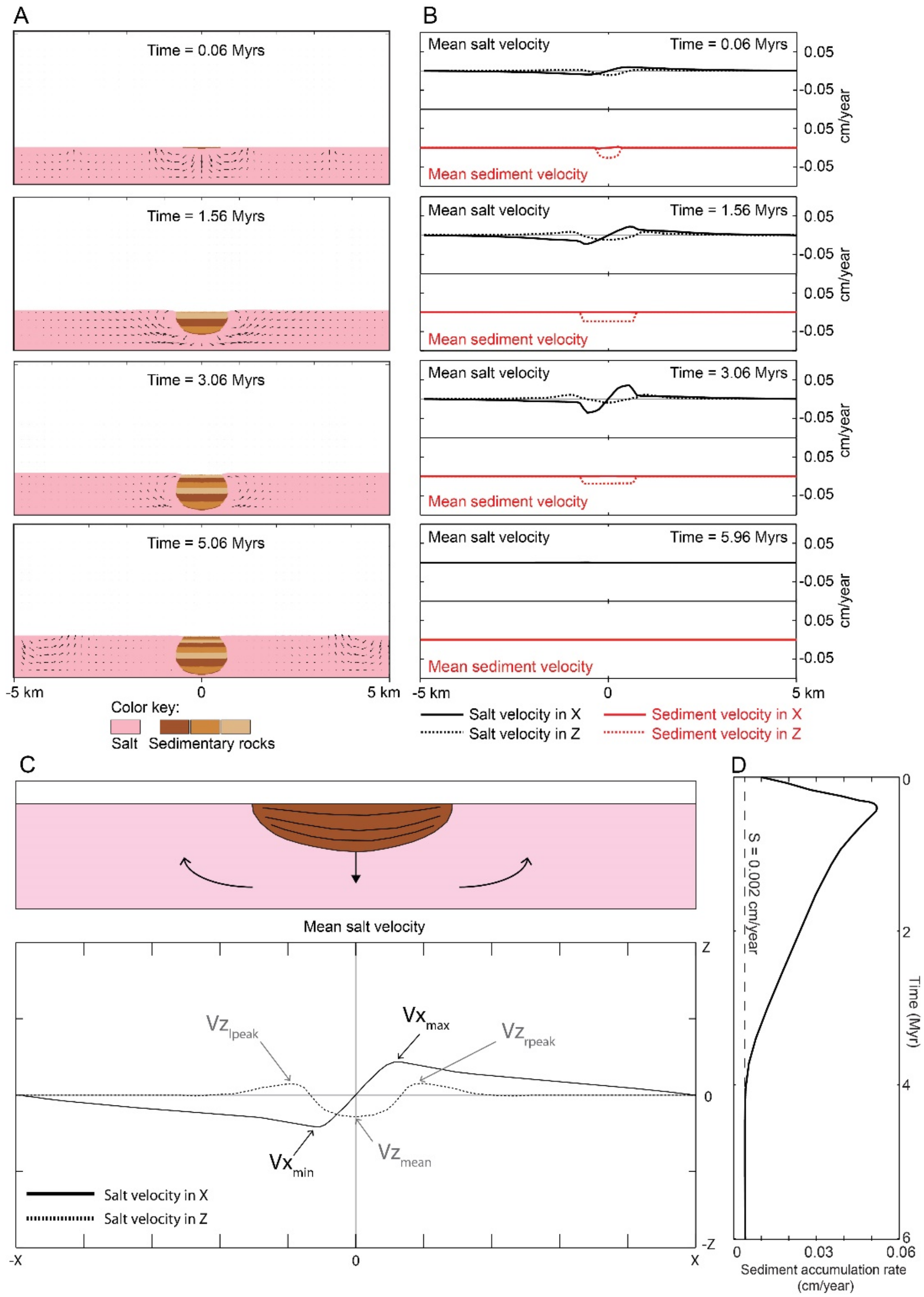

Figure 5. A. Time evolution of simulation 1, which was performed with one seeded minibasin. Velocity vectors are shown in the salt. In this simulation that serves as a control simulation, the imposed "seed" results in an isolated and model-domain-centered minibasin with symmetric stratal geometries. Sediment properties are $C = 0.0$ MPa, $\Phi = 30°$ and $\rho_{sediment}=2500$ kg/m^3. B. Snapshots of the mean velocity values (X and Z components) within the salt (black line) and within the sediments (red line) for same time steps shown in A. C. Schematic plot of the mean velocity values within the salt expected for an isolated subsiding minibasin. The salt evacuated as the minibasin subsides is flowing symmetrically in both directions away from the minibasin, with the peak vertical flow ocurring close to the minibasin. D. Evolution of the sediment accummulation rate in the isolated minibasin of simulation 1.

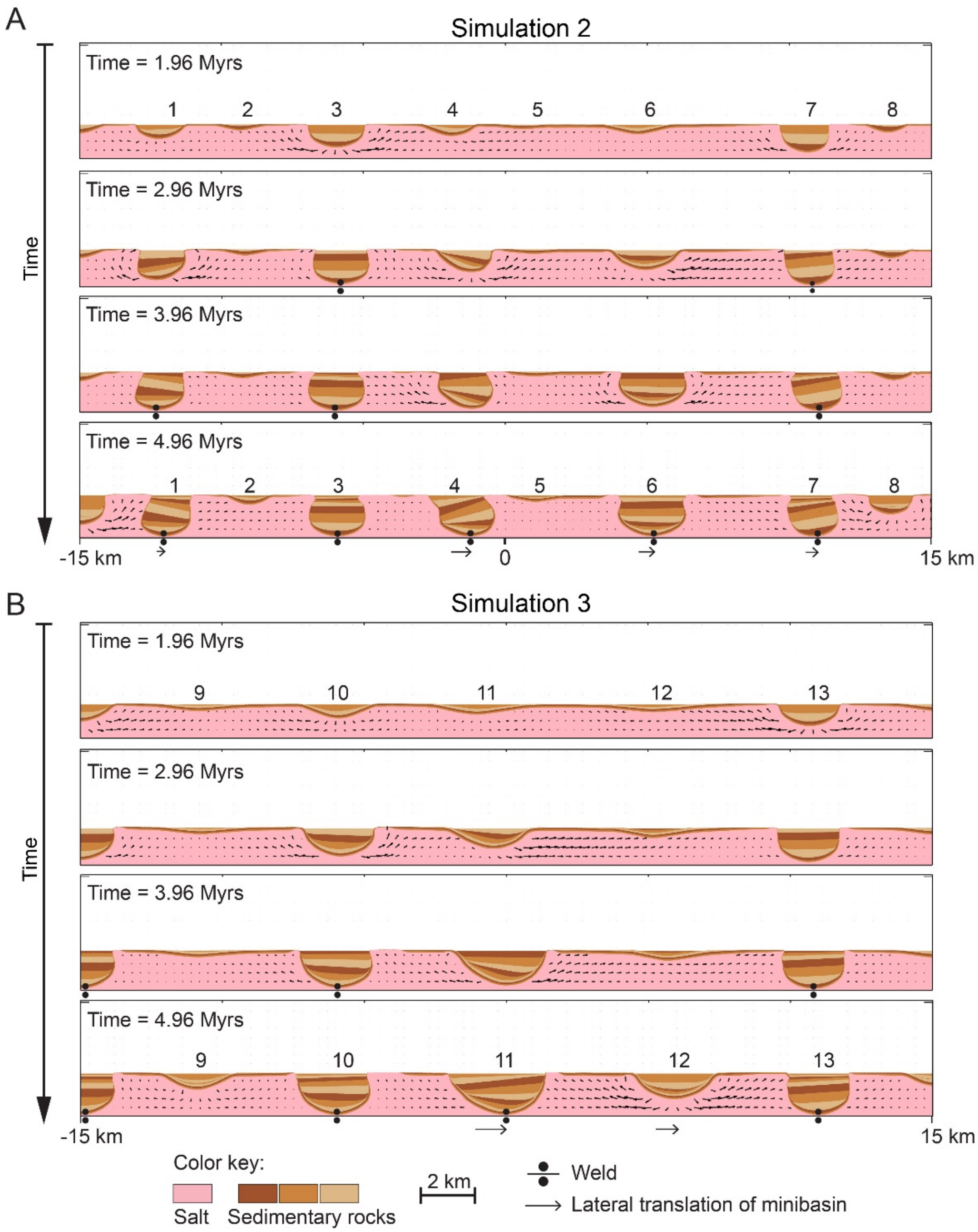

Figure 6. Time evolution of two forward numerical simulations where no pre-kinematic seed was added. Simulations differ in the properties used to model the sediments. Velocity vectors are shown in the salt. In simulation 2 (A), sediments are modelled with C = 0.0 MPa, Φ = 15° and $\rho_{sediment}$=2500 kg/m^3. In simulation 3 (B), sediments are modelled with C = 0.2 MPa, Φ = 10° and $\rho_{sediment}$=2500 kg/m^3. Minibasins form and evolve by density driven subsidence in locations that have not been explicitly predefined. The resulting minibasins are numbered in the lowermost panel that represents the final time step (time = ~5 Myrs.) and in a panel representing an intermediate time step (time = ~ 2 Myrs). One of the main characteristics of these two examples and other similar simulations is the different subsidence rates of the minibasins (minibasins can be initiated at different times) and the resulting complex stratal geometries of the minibasins, including symmetric (e.g. minibasins 3 and 6) and asymmetric geometries (e.g. minibasins 4 and 11).

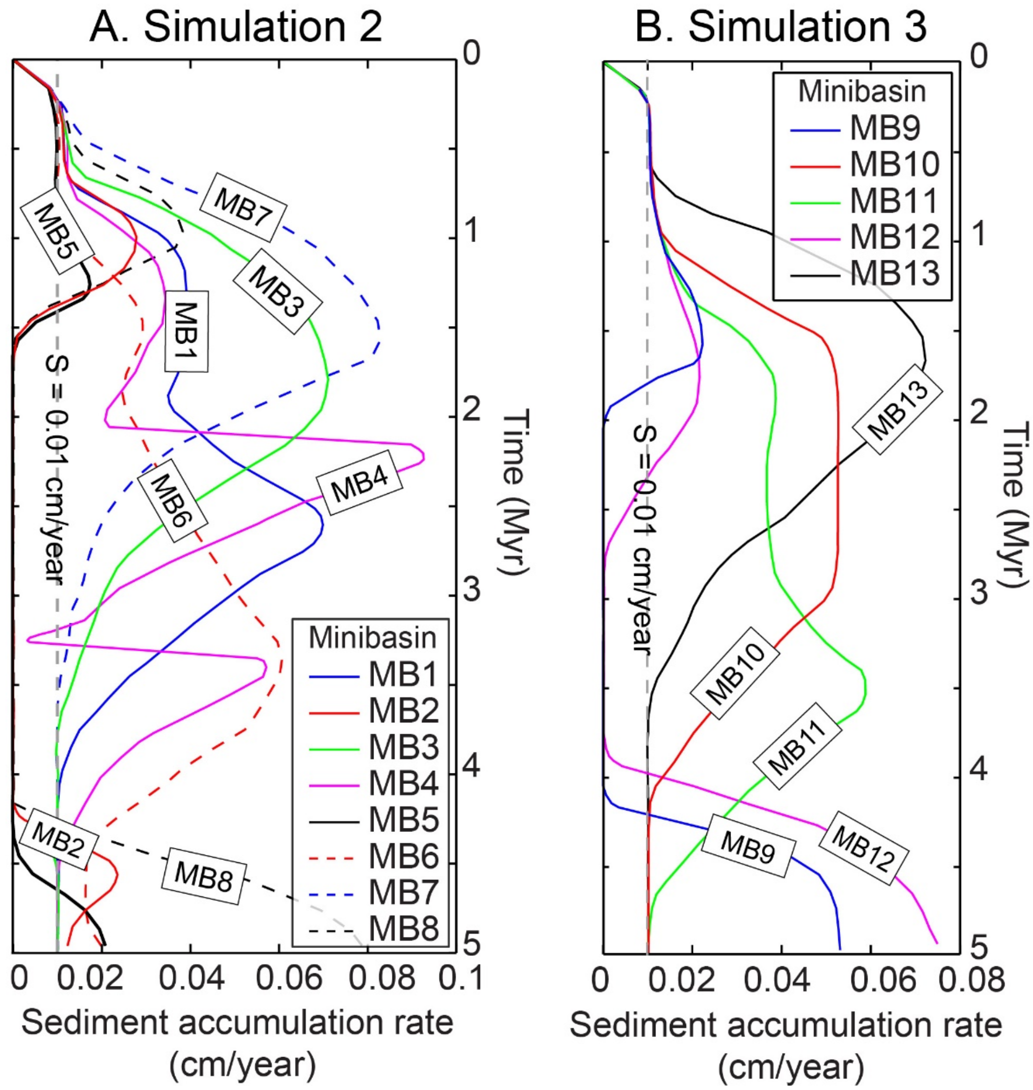

Figure 7. A. Evolution through time of the sediment accumulation rates in the minibasins of simulation 2 (minibasins 1 through 8). B. Evolution through time of the sediment accumulation rates in the minibasins of simulation 3 (minibasins 9 through 13). Note that the sediment accumulation rates in the minibasins of both simulations are very variable through time, ranging from no sedimentation or very low sediment accumulation close to the aggradation rate (S=0.01cm/year), to maximum peak values of 0.05-0.09 cm/year.

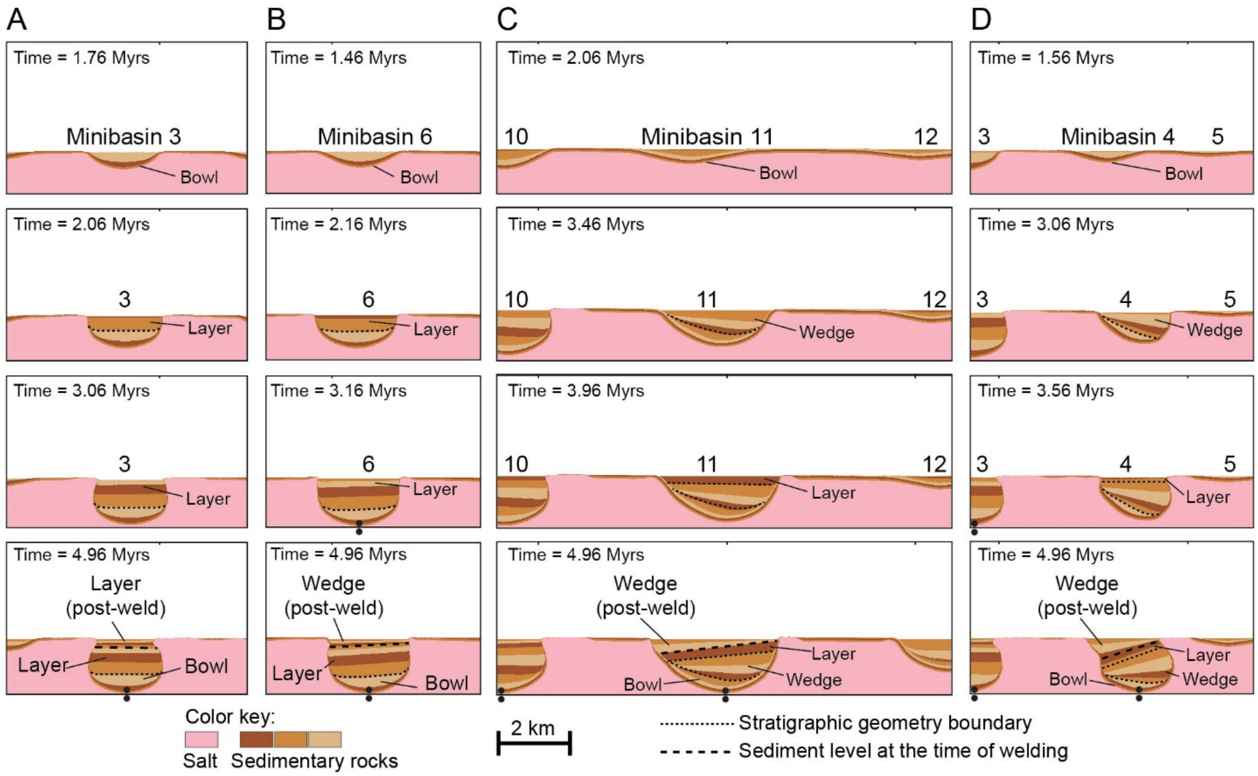

Figure 8. Time evolution of several of the minibasins formed in simulations 2 and 3. Different minibasin geometries, symmetric or asymmetric, can be observed in the simulations. Minibasins 3 and 6 are overall symmetric minibasins (A and B), whereas minibasins 11 and 4 are strongly asymmetric minibasins (C and D). The dashed lines within the minibasins, indicate a change in the stratal geometries (bowl, wedge, layers sensu Weimer and Rowan, 1998) within the minibasins. Dashed thicker black line, indicates the approximate sediment infill level at the time of basal welding of the minibasin. These changes in geometry, correspond with changes in the subsidence style of the minibasins that as described in the text can be linked in some cases to minibasin interactions.

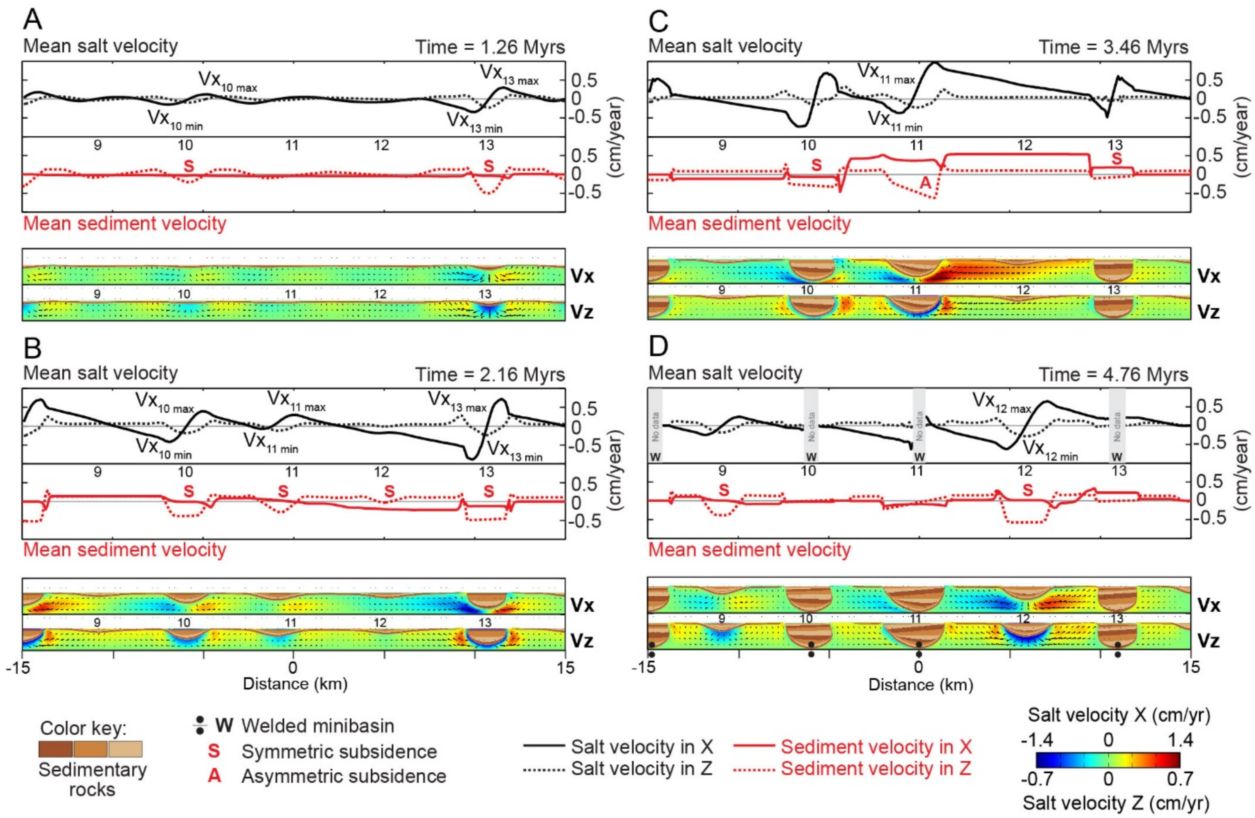

Figure 9. A through D, snapshots of the evolution of simulation 3. Each time step is illustrated with four panels. Upper two panels contain the plots of the mean velocities (X and Z components) within the salt (black line, excluding the sediments) and within the sediments (red line, excluding salt). Lower two panels show the corresponding simulation output, with the sediments colored by the rock phase, and the salt colored by the value of the velocity component (X component for the upper pannel, Z component for the lowe panel) and velocity vectors.

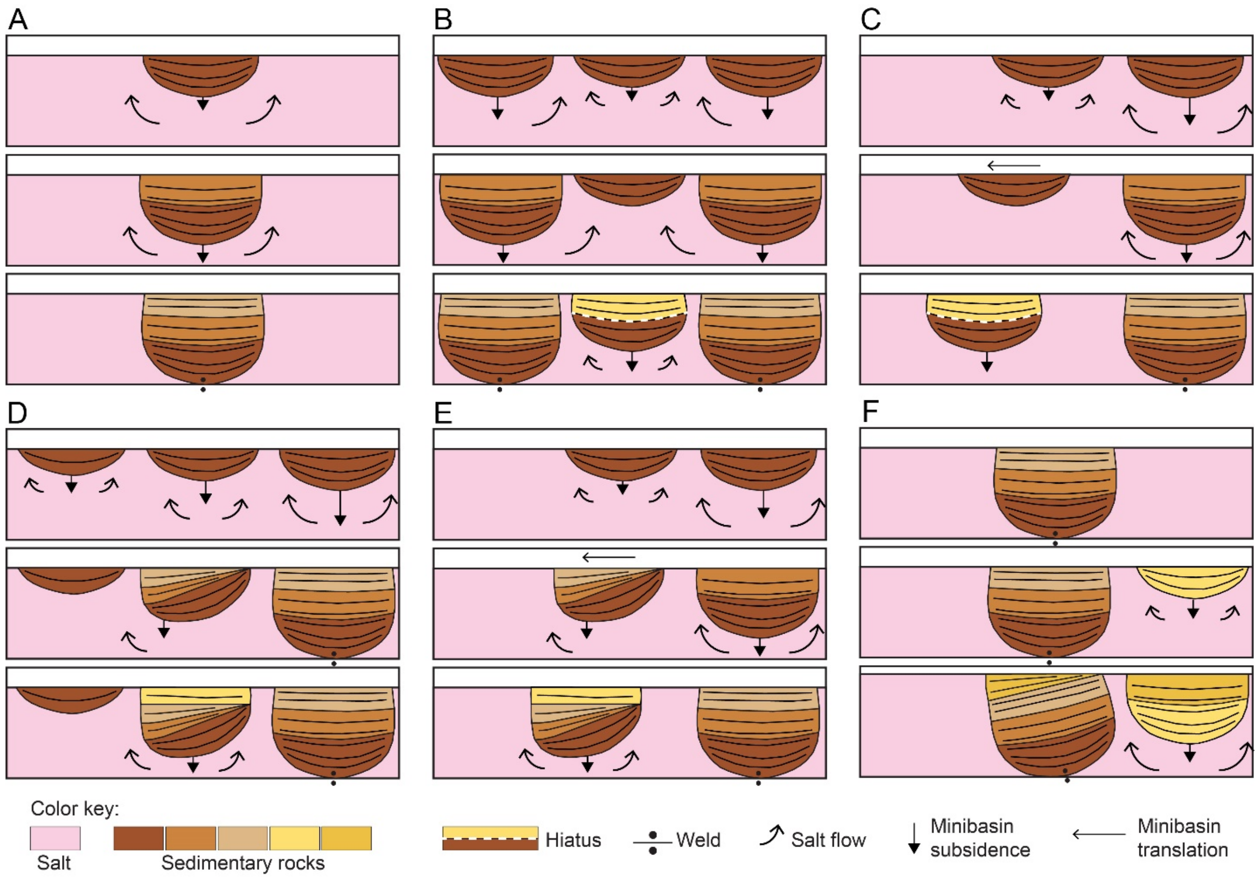

Figure 10. Conceptual sketches of the minibasin interactions observed in the numerical simulations. Minibasin subsidence is indicated by the downwards pointing arrows, whose length is scaled to represent the relative subsidence rate (e.g. longer arrows indicate higher subsidence rate). A. Sketch of a simple scenario in which an isolated minibasin is subsiding vertically. B and C, sketches in which the effect of perturbations in the salt flow induced by adjacent minibasins may lead to preventing one minibasin from subsiding and/or translate it laterally, resulting in a sedimentary hiatus. D, E, F. Sketches illustrating examples of potential interactions between minibasins that would result in differential subsidence histories and asymmetric stratal geometries. See text for details.